



Confined cell migration along extracellular matrix space *in vivo*

Oleksandr Chepizhko^a, Josep-Maria Armengol-Collado^b, Stephanie Alexander^{c,d,1}, Esther Wagena^e, Bettina Weigelin^{e,2}, Luca Giomi^b, Peter Friedl^e, Stefano Zapperi^{f,g,3}, and Caterina A. M. La Porta^{h,i,3}

Affiliations are included on p. 7.

Edited by David Weitz, Harvard University, Cambridge, MA; received July 12, 2024; accepted November 24, 2024

Collective migration of cancer cells is often interpreted using concepts derived from the physics of active matter, but the experimental evidence is mostly restricted to observations made *in vitro*. Here, we study collective invasion of metastatic cancer cells injected into the mouse deep dermis using intravital multiphoton microscopy combined with a skin window technique and three-dimensional quantitative image analysis. We observe a multicellular but low-cohesive migration mode characterized by rotational patterns which self-organize into antiparallel persistent tracks with orientational nematic order. We analyze the deformations induced by the cells in the extracellular matrix and find broadly distributed strain bands with a prevalence of compression. A model of active nematic hydrodynamics is able to describe several statistical features of the experimentally observed flow, suggesting that collective cancer cell invasion can be interpreted as a nematic active fluid in the turbulent regime. Our results help elucidate the migration patterns of cancer cells *in vivo* and provide quantitative guidance for the development of realistic *in vitro* and *in silico* models for collective cell migration.

collective cell migration | extracellular matrix confinement | quantitative image analysis | active nematic turbulence

Cancer cell invasion during metastasis entails cell migration through or along tissue structures (1), primarily driven by actomyosin-independent movement (2, 3). Throughout the invasion stages, cancer cells interact with nonneoplastic tissue (4) comprising both cells and the extracellular matrix (ECM) (5), a complex and dynamic network with hierarchical organization characterized by distinct structural features, including aligned interfaces and clefts. Aligned interfaces are well-defined boundaries between different ECM components, facilitating the alignment of fibers, such as collagen, in a coordinated manner. Clefts along the ECM are narrow spaces or gaps between ECM components that create a specialized microenvironment involved in cell adhesion, migration, and signaling, allowing cells to navigate through the ECM and interact with neighboring cells or structural elements. In addition to aligned interfaces and clefts, multicellular tissue structures also involve perivascular, perimyofiber, and perineural spaces. In particular, perivascular spaces surround blood vessels, provide a specialized environment for cell–ECM interactions, and are involved in regulating vascular permeability, immune cell recruitment, and angiogenesis.

Collective invasion manifests in distinct forms depending on the tumor's characteristics and the surrounding tissue microenvironment. Cohesive and cell-intrinsic invasion is observed predominantly in epithelial tumors, wherein tumor cells maintain their cell–cell adhesion and collective behavior during the invasion process (6). This mode of invasion involves the coordinated movement of cohesive cell clusters which penetrate surrounding tissues. In mesenchymal tumor cell models subjected to high tissue confinement, a multicellular but low-cohesive invasion pattern emerges (7). In such scenarios, tumor cells exhibit reduced cell–cell adhesion, resulting in a more individualized and scattered invasion phenotype. This mode of invasion is influenced by the limited physical space available within the tissue, which restricts collective behavior. Furthermore, gliomas invading the white matter of the brain exhibit a distinct multicellular network-like invasion pattern (8). *In vivo*, mesenchymal melanoma and sarcoma invade collagen-rich deep dermis collectively, as finger-like strands extending up to millimeters along myofibers, vessels, and neural structures (9).

In analogy with amorphous glassy materials (10), cellular assemblies are observed to undergo a jamming transition (11) characterized by a progressive loss of motility which may be driven by an increase in cell density (12, 13), a decrease in active forces (14) or by the loss of intracellular adhesion (15). In particular, experiments *in vitro* showed

Significance

Cancer metastasis involves the collective migration of cancer cells in confined space, a problem that has been widely investigated *in vitro*. Here, we quantify the flow patterns of cancer cell as they invade tissue space and deform the surrounding extracellular matrix *in vivo*. Cell motion self-organizes into well-defined traffic lanes aligned along interstitial tracks and resembles the flow of a turbulent active fluid. Our study provides insights into the mechanisms underlying tumor invasion and sheds light on physical factors contributing to metastatic spread.

Author contributions: P.F., S.Z., and C.A.M.L.P. designed research; O.C., J.-M.A.C., S.A., E.W., B.W., L.G., P.F., S.Z., and C.A.M.L.P. performed research; O.C., S.Z., and C.A.M.L.P. analyzed data; L.G. designed the model; and P.F., S.Z., and C.A.M.L.P. wrote the paper.

The authors declare no competing interest.

This article is a PNAS Direct Submission.

Copyright © 2024 the Author(s). Published by PNAS. This article is distributed under Creative Commons Attribution-NonCommercial-NoDerivatives License 4.0 (CC BY-NC-ND).

¹Present address: European Molecular Biology Laboratory Imaging Centre and Cell Biology and Biophysics Unit, European Molecular Biology Laboratory, Heidelberg 69117, Germany.

²Present address: Department of Preclinical Imaging and Radiopharmacy, Eberhard Karls University, Tübingen 72076, Germany.

³To whom correspondence may be addressed. Email: stefano.zapperi@unimi.it or caterina.laporta@unimi.it.

This article contains supporting information online at <https://www.pnas.org/lookup/suppl/doi:10.1073/pnas.2414009121/-DCSupplemental>.

Published December 30, 2024.

that cell density regulation by matrix confinement plays a crucial role in controlling collective movement (16, 17) and that downregulation of adherens junctions leads to a change from coordinated to uncoordinated collective cell migration (16) which was interpreted as a nonequilibrium phase transition from laminar active nematics (18) to turbulent active fluid flow (19). Alternative models of collective cell invasion include leader–follower systems (20, 21) or models where cells exhibit differential adhesion with other cells (22, 23).

The biomechanics and coordination mechanisms underlying mesenchymal collective invasion of tumor cells *in vivo* remain largely unexplored. Consequently, the predictions made by the unjamming paradigm, which considers tumor cells as active nematic fluid (18, 24), have yet to be thoroughly tested in three-dimensional (3D) models *in vivo* settings. Specifically, it remains unclear whether and under what conditions tumor cells exhibit laminar or turbulent streaming as they navigate through the tissue. Furthermore, various aspects of the phase transition, such as the individualization of cells into single entities, the occurrence of jamming, and the potential for migration arrest, require further investigation. Understanding these phenomena would provide valuable insights into the dynamic behaviors of tumor cells during invasion and metastasis. To address these gaps in knowledge, analyses of cell fluxes in 3D models and *in vivo* tissues using advanced imaging techniques are necessary. By elucidating the biomechanical principles and intricate coordination mechanisms involved in tumor cell invasion, we can gain a deeper understanding of the main components of metastatic cancer progression.

The purpose of the present study is to investigate cell dynamics during the collective invasion of metastatic sarcoma tumors into the deep dermis using intravital multiphoton microscopy combined with a skin window technique. By employing this approach, we aim at capturing the real-time behavior of individual cells in three dimensions *in vivo* and quantify their progression over time using image analysis. A theoretical model, based on active nematic hydrodynamics (25), is then employed to rationalize the statistical properties of the observed cellular flow and highlight the crucial role of confinement for collective invasion. By applying these analytical tools to our *in vivo* model, we aim to gain insights into the mechanisms underlying tumor invasion and potentially shed light on the factors contributing to the metastatic spread of sarcoma. This study represents an important step toward understanding the complex dynamics of tumor progression in a more physiologically relevant context, supporting the concept of cancer invasion following principles of an active fluid with turbulent flow fields penetrating between solid tissue structures.

Results

Migrating Cancer Cells Display Antiparallel Flow Patterns and Vorticity. In Fig. 1*A*, we report a typical projected image of the collective organization of mesenchymal cancer cells as they invade interstitial tissue in the deep mouse dermis *in vivo* (see also *SI Appendix*, Fig. S1*A*). Using the 3D optical flow algorithm discussed in *Materials and Methods*, we analyze the local velocity signal obtained from the position of the nucleus and the cell body (cytoplasm) from the sequence of 3D image stacks and extract its distribution over time. The velocity distributions of the nucleus and cell body are similar although the nuclei show slightly larger mobility (*SI Appendix*, Fig. S2). The distribution of the individual components of the velocities for the nuclear signal

are reported in Fig. 1*B* in a semilogarithmic scale which highlights the non-Gaussian, exponential decay of the distribution tails. The largest velocity component is along the *x*-direction which is close to the alignment direction of the interstitial structures detected by second harmonic generation (SHG), including collagen bundles (Fig. 1*A*, in magenta) and myofibers. This is also illustrated in *SI Appendix*, Fig. S2 *D–F* with an example. The velocity distributions depend very little on time (*SI Appendix*, Fig. S3).

By inspecting the amplitude (*SI Appendix*, Fig. S1) and directionality (Fig. 1*C*) of flow patterns, quantified as instantaneous spatial localization of the cell velocities, trajectories segregate into principal, anterograde, or retrograde directions parallel to the interstitial tissue structures, with large regions moving in one direction coexisting with other regions moving in the opposite one (see also *Movies S1–S4*).

We also analyze the flow patterns from the point of view of internal rotations as quantified by the vorticity field $\vec{\omega} = \nabla \times \vec{v}$ and the angular velocity $\Omega = \frac{1}{2}\hat{\vec{v}} \cdot \nabla \times \vec{v}$, where $\hat{\vec{v}} = \vec{v}/|\vec{v}|$. We report in Fig. 1*D* the spatial organization of the angular velocity for the nuclear signal. The images show that upon changing direction, the movement of adjacent nuclei maintains low correlation to neighboring nuclei. The distribution of the angular velocities is reported in Fig. 1*E* for the individual components of the nuclear signal (for the cytoplasmic signal, see *SI Appendix*, Fig. S4). We observe non-Gaussian exponential tails and notice that vorticities are almost isotropic since the distributions depend only slightly on the direction of the rotational axis considered. These rotational patterns are similar and reminiscent of the uncoordinated flow patterns of collectively moving breast cancer cells after down-regulating E-cadherin (16).

To further investigate how stable in time are the antiparallel flow patterns illustrated in Fig. 1*C*, we consider the component of the velocity $v_{||}$ parallel to the interstitial tracks and examine its persistence which quantifies how often the local flow velocity is anterograde or retrograde. In practice for each pixel of the image sequence, we measure the fraction of time steps in which the local velocity $v_{||}$ is larger than a threshold v_c and subtract the fraction of time steps in which it is smaller than $-v_c$. This produces a persistence parameter $-1 \leq \phi(x, y, z) \leq 1$ whose localization is reported in Fig. 2*A* for a typical measurement of the nuclear signal (see also *SI Appendix*, Fig. S1*B*). The cytoplasmic signal yields similar results. Flow fields of cancer cells are localized in persistent tissue regions, with velocity orientation mostly parallel (Fig. 2*A*, red zone) or antiparallel (Fig. 2*A*, blue zone) to connective tissue structures. The duration of persistent flow is summarized in Fig. 2*B* where we report the distribution of the duration τ of persistent events, defined as the amount of time for which the flow in each pixel occurs along the same direction. Typical persistence times in subregions of the invasion zone span a few hours. The fact that persistence decays in time indicates that cell velocities eventually change directions.

Collective Cell Migration Is Quantitatively Described by a Model of Active Nematic Turbulence. Flowing multicellular systems often leverage on liquid crystal order, either polar or nematic, to focus microscopic forces and achieve mechanical functionality at mesoscopic length scales. To test whether this mechanism is at play in our *in vivo* model, we quantify nematic order by computing the local orientation $\vec{n} = \cos \theta \hat{x} + \sin \theta \hat{y}$ of the cell nuclei as a function of time (Fig. 3*A*). Selecting only the region within individual channels, we reveal that the stream lines associated with the orientation map are predominantly directed

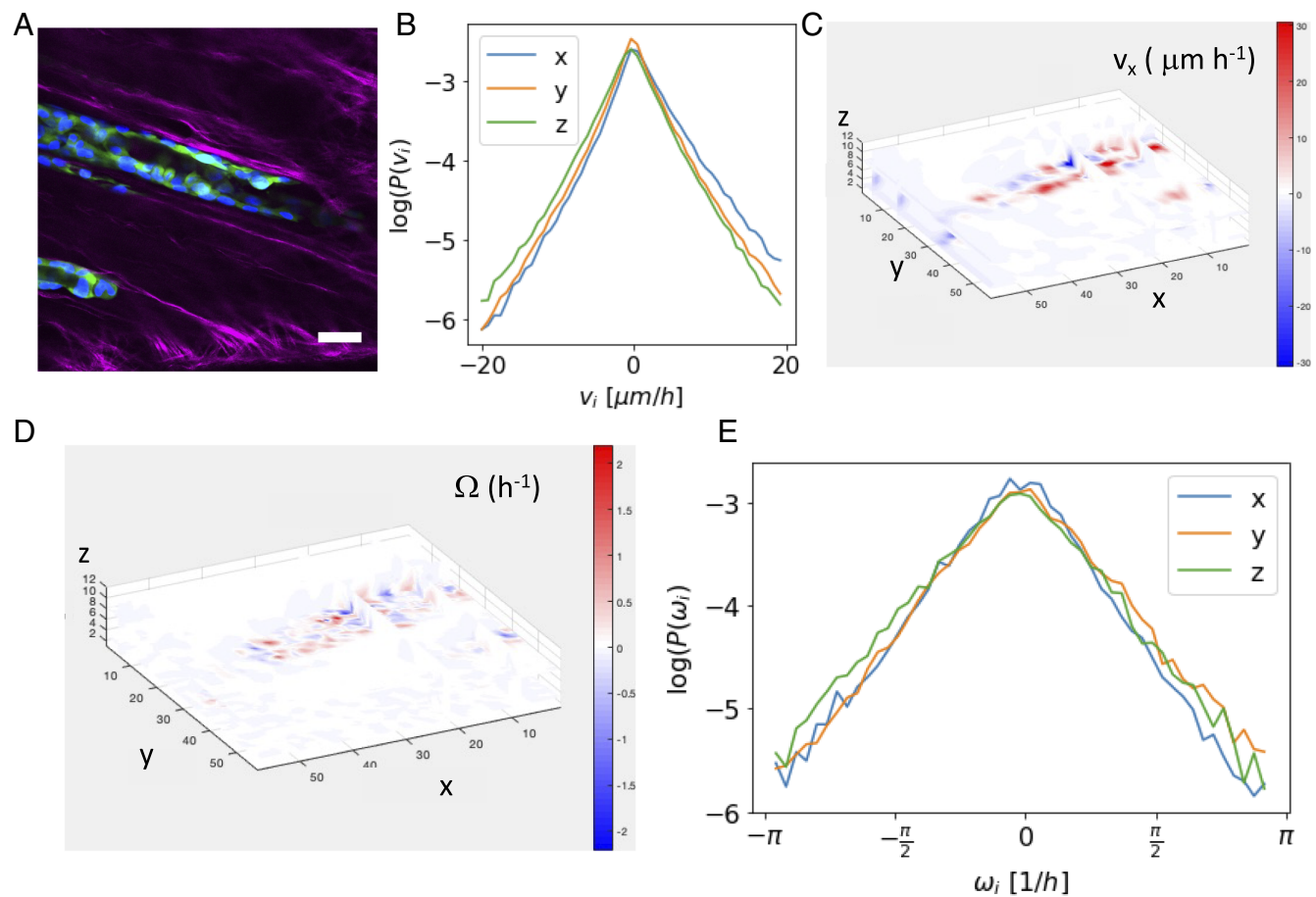


Fig. 1. Migration of cancer cells *in vivo* exhibits non-Gaussian velocity and vorticity distributions. (A) Snapshot of collectively invading HT1080 cells in the mouse dermis. Colors are: cytoplasm in green, nuclei in blue and collagen in magenta. (Scale bar, 50 μm .) (B) The 3D profile of the x component of the velocity extracted from the nuclear signal. (C) The velocity distributions for the different spatial components (nuclear signal) shows a prevalence across the positive x direction, corresponding approximately to the flow direction, but significant motion also occurs across the opposite direction. The difference between the distributions of the x and y, z components of the velocity is statistically significant according to the Kolmogorov-Smirnov test ($P < 10^{-8}$). (D) The angular velocity field for cancer cells computed from the nuclear signal. (E) The vorticity distributions for the different spatial components. Differences among components are small but statistically significant ($P < 10^{-8}$).

along the flow direction, with topological defects mostly located close to the boundary of the channel (Fig. 3B and Movie S5). This is also confirmed by the distribution of the local orientation θ , i.e.,

$P(\theta)$, which is peaked along the direction of the flow (Fig. 3C), and the nematic order parameter, i.e., $Q = 2\langle[\cos(\theta - \langle\theta\rangle)]^2\rangle - 1$, which is close to one for all times (Fig. 3D).

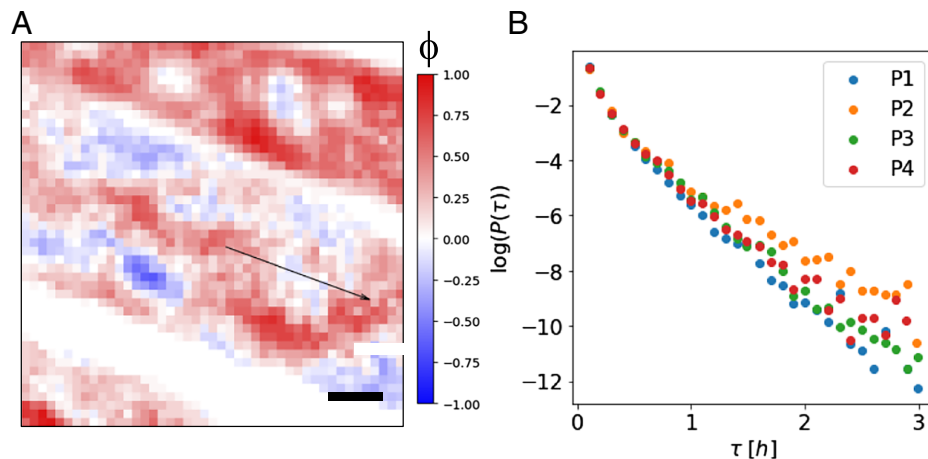


Fig. 2. Collective cancer cell migration displays persistent lanes. (A) Map of the persistence parameter ϕ defined as the fraction of time that at a given location (pixel) the velocity projected along the flow direction (denoted by an arrow) is positive and larger than a threshold v_c minus the fraction of time that the velocity is less than $-v_c$. (Scale bar, 50 μm .) (B) Distribution of persistent times τ , defined as the duration for which the projected velocity at a pixel v_i is continuously such that $|v_i| > v_c$. The analysis is performed on the nuclear signal.

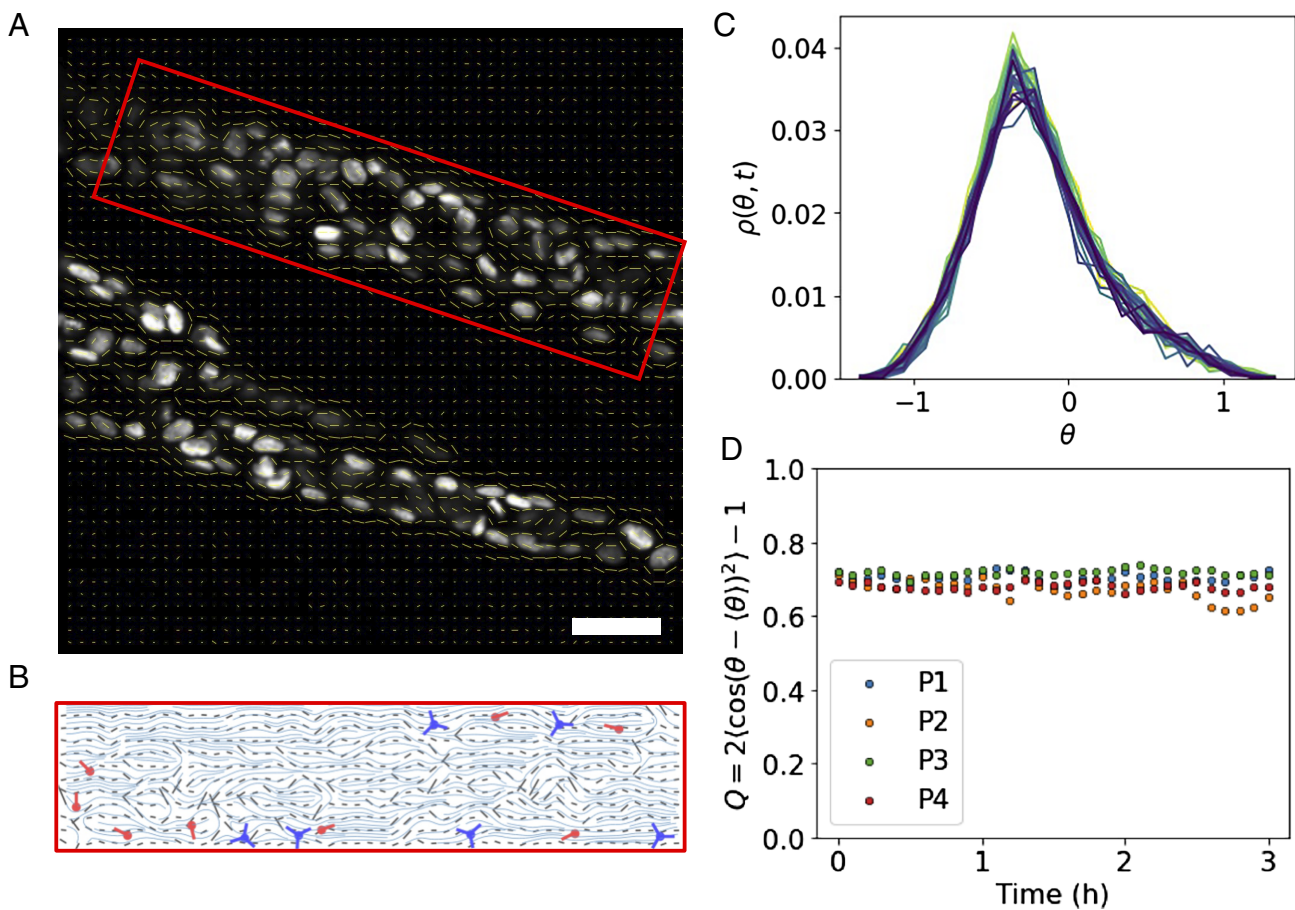


Fig. 3. Migrating nuclei display nematic order. (A) Snapshot of the cell nuclei where local orientation vectors are superimposed. (Scale bar, 50 μm .) (B) Topological defects associated with the channel highlighted in red. (C) Distributions of the orientation angle for different time frames. (D) The time-dependence of the nematic order parameter as a function of time, for different experimental measurements.

To shed light on how nematic order affects the spatiotemporal dynamics of collective invasion, we numerically integrate the equations of active nematic hydrodynamics in a channel with no-slip walls (see *SI Appendix* and *SI Appendix*, Fig. S5 for details on the model and simulations methods). For computational convenience, we simulate the invasion process in two dimensions, but, as we explain in *SI Appendix*, the same results qualitatively hold in three dimensions. When assuming that cancer cells are extensile as suggested by experiments *in vitro* (26), simulations reveal a regime of active nematic turbulence with transient but long-lived periods of directional flow. The statistical features of the simulated flow are in excellent agreement with experimental observations: the turbulent flow (Fig. 4A) displays non-Gaussian velocity (Fig. 4B) and vorticity distributions (Fig. 4C) in close analogy with experiments. We notice that the velocity distribution develops non-Gaussian tails only in the limit of small channel width h (Fig. 4B), highlighting the role of confinement. In Fig. 4, h is expressed in units of the so-called active length scale ℓ_a (25), corresponding to the distance at which the active torques, generated by the cells, and the passive torques, resulting from their excluded-volume interactions, balance each other (see *SI Appendix* for more details). This is estimated to be $\ell_a \approx 5 \mu\text{m}$ for our system (see *SI Appendix* for more details) so that experimentally measured channel widths correspond to the lowest value of the simulated channels. The nonslip boundary conditions imposed in the simulations produce a large peak in the velocity at $v_x = 0$ (*SI Appendix*, Fig. S6) which disappears when the distribution is sampled in the central region of the

channel (Fig. 4B). The shape of the distribution of local persistent times is also in agreement with experiments and shows that its characteristic time scale is controlled by the channel width h (Fig. 4E). Furthermore, the spatial arrangement of local orientations (Fig. 4F) and its distribution (Fig. 4G) display patterns that are again in close agreement with experiments (Fig. 3).

Extracellular Matrix Deformation Is Prevalently Compressive. A crucial assumption of our theoretical model is that cells behave extensile, thus compressing the surrounding extracellular matrix. To verify this assumption, we characterize the deformation of the extracellular matrix induced by cell migration by considering the collagen signal. Cancer cell flow proceeds mainly along directions corresponding to the direct interaction with interstitial structures, specifically fibrillar collagen detected by the SHG signal (Fig. 1A, magenta). We thus project collagen deformations along the parallel and perpendicular directions with respect to the migration direction, as illustrated in Fig. 5A which reports an example of the collagen displacements for a typical configuration. The tensile/compressive strain fields (Fig. 5B, red/blue, respectively) along the perpendicular direction ($\epsilon_{\perp,\perp} = \frac{\partial u_\perp}{\partial x_\perp}$) are reported in Fig. 5B, while strain along the parallel direction ($\epsilon_{\parallel,\parallel} = \frac{\partial u_\parallel}{\partial x_\parallel}$) are reported in *SI Appendix*, Fig. S7, which also reports shear strain patterns. The maps reveal extensive strain bands running parallel to the invasion direction, while shear strain patterns are more localized (*SI Appendix*, Fig. S7). A quantification of the strain indicates a prevalence

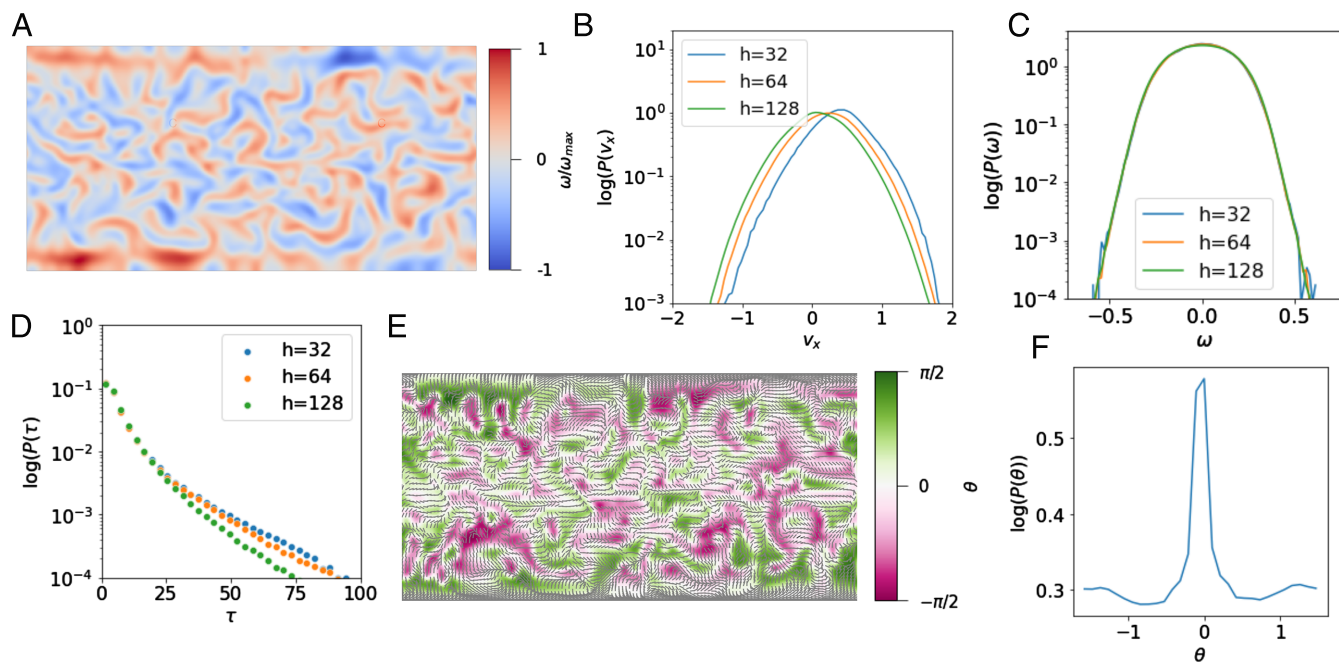


Fig. 4. Model of active nematic turbulence describes collective cell migration in vivo. (A) The vorticity field obtained from the simulation of the active nematic model. (B) The distributions of velocities along the flow direction, obtained excluding the boundary layer (see also *SI Appendix*, Fig. S6). (C) The distributions of vorticities and (D) the distribution of persistence times for different channel widths h , resulting from the simulations. (E) A map of the orientation field and (F) the distribution of local orientation angle obtained from simulations. In all the panels, all quantities are expressed in dimensionless units as described in *SI Appendix*.

of compressive strain over tensile strain in the collagen, $\langle \epsilon_{\perp,\perp} \rangle = -0.006 \pm 0.001$ and $\langle \epsilon_{||,||} \rangle = -0.015 \pm 0.001$, confirming that on average cells behave as an *extensile* active system as assumed in the model, compressing the surrounding collagen. The distribution of the displacements along the three directions is reported in Fig. 5D, and the distribution of the absolute value of the strain is reported in Fig. 5E. The distributions display broad tails decaying as power laws with exponent close to $\alpha = 3.5$. Similar power-law strain distributions are observed in defected crystals where the exponent is expected to be $\alpha = 3$ (27).

Discussion

In this paper, we used intravital multiphoton microscopy combined with a skin window technique to investigate the dynamics of individually and collectively moving cells injected into the deep dermis of a mouse. The main purpose of our study was to assess the relevance within an *in vivo* setting of general concepts commonly used to interpret experiments on collective cell migration and invasion performed *in vitro*. In this context, a widely applied framework is provided by the jamming-unjamming transition according to which cells collectively switch from a state of limited mobility to a flowing state in response to changes in their internal and external conditions, including for instance cell density, adhesion strength, mechanical stresses, substrate conditions, and cell contractility. Cell behavior is usually summarized by phase diagrams inferred from experiments (11, 13, 14, 16) and numerical simulations (13, 28–30) which illustrate the dependence of cell dynamics on a relevant set of biophysical and biochemical parameters. Recent experiments showed that cancer cells in a spheroid respond to changes in the expression of intracellular adhesion molecules and in the density of the collagen medium by undergoing a dynamic transition from an active laminar nematics phase, where the motion is

coordinated and oriented, to a turbulent phase, characterized by extensive vorticity (16).

In our experiments, the collective flow of cancer cells was confined by interstitial tissue structures and ECM which induced intriguing dynamic behavior within the active fluid phase. In particular, cell flow was observed to self-organize into persistent antiparallel cell tracks which are reminiscent of similar patterns observed *in vitro*. The formation of organized flow patterns due to confinement or geometry is a well-established phenomenon in active matter (12, 18, 31). In particular, recent cell migration experiments *in vitro* revealed the formation of antiparallel streams induced by the micropatterned grooved substrate (32).

The flow patterns observed *in vivo* were reproduced by a model of active nematic turbulence (25), which predicted that persistent times should decrease as the channel width increases, highlighted the relevance of confinement. This prediction was confirmed by experiments where the persistent times observed in narrow channels (P2/P4) are longer than those observed in wider channels (P1/P3). The combination of experiments and theory demonstrated that collective cell invasion *in vivo* occurs in the turbulent regime, suggesting that confinement and moderate to low intercellular adhesion, which is characteristic of mesenchymal cancer cells, are promoting the partial disruption of nematic order and the onset of turbulent flow. Furthermore, our results suggested that tissue confinement by ECM provides cues that are able to organize cellular flow. We thus analyzed in more depth the interactions between migrating cells and ECM by studying the deformation patterns induced in the collagen by the cells. We observed well-organized deformation bands extending in the direction parallel to the flow. While strain on collagen fibers includes both tensile and compressive components, the compressive part is stronger indicating that cancer cells are extensile and push on the ECM. This observation confirms a crucial assumption of the active hydrodynamic model. Furthermore, cells induce in the ECM strain distributions displaying “fat tails,” decaying

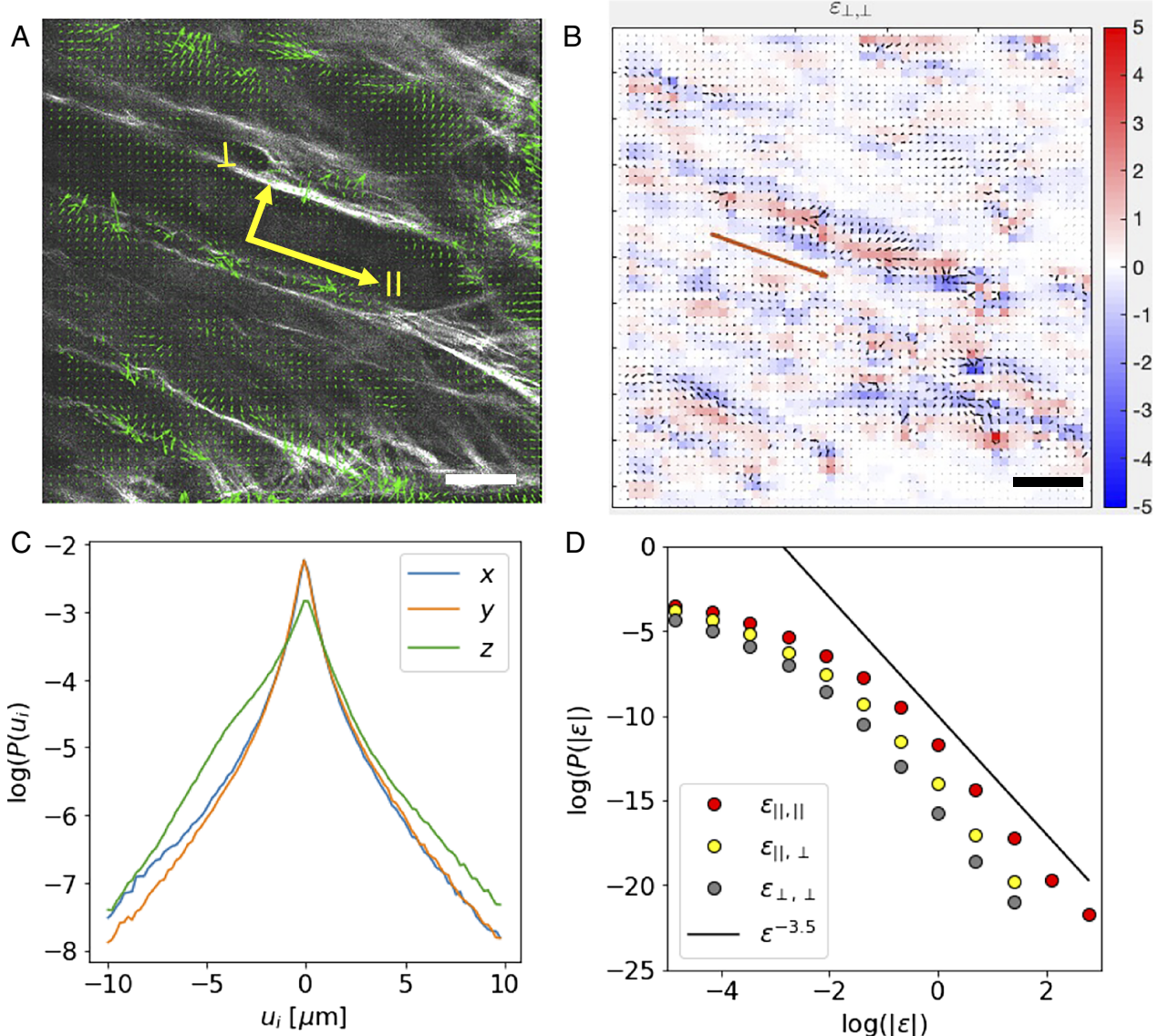


Fig. 5. Collective cancer cell migration induces collagen deformation. (A) A typical map of collagen displacements, indicating also the directions parallel (\parallel) and perpendicular \perp to the flow. (B) The corresponding map of collagen strain fields perpendicular to the flow $\epsilon_{\perp,\perp}$, showing alternation of compressive and tensile bands. (C) The distribution of collagen displacements. (D) The distribution of strain in log-log plot, displaying power-law tails. (Scale bars, 50 μm .)

as power laws, which are reminiscent of the strain distributions observed in crystalline materials in presence of randomly arranged topological defects (27). This analogy suggests that the local deformations induced by cells on neighboring collagen fibers have long-range effects, similar to those induced by dislocations in crystals.

In conclusion, our study represents an important step toward understanding the complex dynamics of confined collective cell migration in a physiologically relevant three-dimensional context. Our analysis provides quantitative measurements *in vivo* of biophysical parameters such as characteristic cell velocities and vorticities, collagen displacements, and strains that can be used as a benchmark to develop more realistic theoretical, computational, and *in vitro* models of collective cell migration.

Materials and Methods

Intravital Microscopy of Tumor Cell Invasion. Titanium dorsal skin imaging windows were transplanted onto 10- to 14-wk-old male athymic Balb/c nude mice (CANN.CG-FOXN1NU/CRL, Charles River), as described (33). One day

postsurgery, HT-1080 tumor cells (5×10^5 in 4 μL PBS) stably expressing nuclear H2B-EGFP and cytoplasmic DsRed2 were implanted into the dermis by image-guided microinjection. For time-lapse recording of tumor cell migration, mice were anesthetized with isoflurane and stably mounted onto a temperature-controlled platform (37 °C). Progression of dual-color tumors was monitored using longitudinal intravital multiphoton microscopy (MPM, LaVision BioTec) (34). Migration modes and efficiency were recorded by subcellular-resolved multiphoton time-lapse microscopy using a 20x objective (NA 0.95, Olympus) at day 7 for up to 4 subregions per tumor. Sequential 4D image series (xyz & time) for up to 300 μm penetration depth at 7 μm step interval and 6 min time interval were recorded for approximately 4 h. The mice were kept hydrated through s.c. injections of 0.9% NaCl solution (Braun) while obtaining image sequences. The excitation wavelengths were 1,090 (DsRed2, SHG) and 910 nm (eGFP). The emission ranges were 535/50 (green), 605/70 (red), and 710/75 (far-red).

Three-Dimensional Optical Flow Algorithm. To analyze the image stacks and obtain the associated velocity and deformation fields in 3D, we implement a 3D version of the classical Horn-Schunck flow algorithm (35). The Horn-Schunck algorithm assumes smoothness in the flow and tries to minimize distortions in the flow. This is done formulating the

flow in terms of a global energy functional which is then minimized. The energy function associated to the three-dimensional image streams is given by

$$E = \int \left[(I_x v_x + I_y v_y + I_z v_z + I_t)^2 + \alpha^2 (|\nabla v_x|^2 + |\nabla v_y|^2 + |\nabla v_z|^2) \right] dx dy dz \quad [1]$$

where I_x , I_y , I_z , and I_t are the derivatives of the image intensity values along the x , y , z and time dimensions, respectively, $\vec{v} = [v_x(x, y, z), v_y(x, y, z), v_z(x, y, z)]$ is the unknown velocity vector, and the parameter α is a regularization constant that controls the smoothness of the flow. In the present implementation, we set $\alpha = 1$. The energy function can be minimized by solving the associated multidimensional Euler–Lagrange equations that are discretized and solved numerically.

Using the flow algorithm described above, we obtain the time-dependent velocity fields $\vec{v}(x, y, z)$, separately for nuclei and cytoplasm. We can then compute the following quantities to characterize the flow: the absolute value of the local velocities $|\vec{v}|$; the velocity along the x , y , z directions v_x , v_y , and v_z ; the velocity along the flow direction defined for each sample as $v_\theta = v_x \cos \theta + v_y \sin \theta$, where $\theta = 10 - 20$ deg is the angle that the stripes occupied by cells make with the x axis; the vorticity $\omega = \nabla \times \vec{v}$ and the angular velocity $\Omega = \hat{v} \cdot \nabla \times \hat{v}/2$; the persistence of the flow direction, estimating for each voxel the fraction of the time in which $v_\theta > v_t$ and the fraction of the time in which $v_\theta < -v_t$, where v_t is a threshold used to filter the low velocity noise, and obtaining for each voxel a persistence $-1 < \Phi(x, y, z) < 1$ that quantifies how much the flow across the voxel x , y , z is persistent in the positive or negative direction; the persistence time distribution, computing for each pixel the time intervals τ for which the velocity is persistent, according to the definition above.

Orientations. The orientation distribution is obtained processing the nuclear signal with the ImageJ software using the OrientationJ plugin (36). Streamlines and topological defects are obtained using actempy (<https://github.com/joshchaitanya3/actempy>) (37).

Collagen Deformation. To extract the collagen deformation, a small variation of the optical flow algorithm is used. In the original algorithm, two consecutive images are compared to extract a 3D map of velocities. In the case of deformation, we always fix the first frame as a reference point. Thus, the comparison of each frame is always done with respect to this first frame. We get time-dependent displacements as an output of this algorithm.

Data, Materials, and Software Availability. All study data are included in the article and/or [supporting information](#).

ACKNOWLEDGMENTS. This work was supported by the European Research Council (617430-DEEPINSIGHT) and NIH U54 CA261694-01, and NWO 024.005.009 IMAGINE! to P.F. J.-M.A.-C., L.G., and P.F. acknowledge financial support from NWO-Science-XL 2019.022. L.G. was supported by the European Research Council (865375-HexaTissue). C.A.M.L.P. acknowledges funding from FAIR–Future Artificial Intelligence Research: Adaptive AI methods for Digital Health” Grant No. PNRR_BAC24GVALE_01 PE_0000013, CUP D53C2200238000 and from AIRC under Next Gen Clinician Scientist 2022–ID. 28402 project–P.I. Carlotta Palumbo. S.Z. was supported by Ministero dell’Università e della Ricerca through the PRIN 2022 project METACTOR.

Author affiliations: ^aLakeside Labs GmbH, 9020 Klagenfurt, Austria; ^bInstituut-Lorentz, Universiteit Leiden, 2300 RA Leiden, The Netherlands; ^cDavid H. Koch Center for Applied Research of Genitourinary Cancers, Department of Genitourinary Medical Oncology, The University of Texas MD Anderson Cancer Center, Houston, TX 77230-1439; ^dDepartment of Dermatology and Rudolf Virchow Center, Deutsche Forschungsgemeinschaft Research Center for Experimental Biomedicine, University of Wuerzburg, 97080 Wuerzburg, Germany; ^eDepartment of Medical Biosciences, Sciences, Radboud University Medical Centre, 6525 GA Nijmegen, The Netherlands; ^fCenter for Complexity and Biosystems, Department of Physics, University of Milan, 20133 Milan, Italy; ^gIstituto di Chimica della Materia Condensata e di Tecnologie per l’Energia, Consiglio Nazionale delle Ricerche, Milan, Italy; ^hCenter for Complexity and Biosystems, Department of Environmental Science and Policy, University of Milan, 20133 Milan, Italy; and ⁱUnità Operativa Complessa Maxillo-Facial Surgery and Dentistry Fondazione Istituto di ricovero e cura a carattere scientifico Ca’ Granda, Ospedale Maggiore Policlinico di Milano, 20122 Milan, Italy

1. P. G. Gritsenko, O. Ilina, P. Friedl, Interstitial guidance of cancer invasion. *J. Pathol.* **226**, 185–199 (2012).
2. A. J. Ridley *et al.*, Cell migration: Integrating signals from front to back. *Science* **302**, 1704–1709 (2003).
3. L. Beunk *et al.*, Actomyosin contractility requirements and reciprocal cell-tissue mechanics for cancer cell invasion through collagen-based channels. *Eur. Phys. J. E* **45**, 48 (2022).
4. G. Charras, E. Sahai, Physical influences of the extracellular environment on cell migration. *Nat. Rev. Mol. Cell Biol.* **15**, 813–824 (2014).
5. F. Rosso, A. Giordano, M. Barbarisi, A. Barbarisi, From cell–ECM interactions to tissue engineering. *J. Cell. Physiol.* **199**, 174–180 (2004).
6. C. Carmona-Fontaine *et al.*, Complement fragment C3a controls mutual cell attraction during collective cell migration. *Dev. Cell* **21**, 1026–1037 (2011).
7. A. Haeger, M. Krause, K. Wolf, P. Friedl, Cell jamming: Collective invasion of mesenchymal tumor cells imposed by tissue confinement. *Biochim. Biophys. Acta (BBA), Gen. Subj.* **1840**, 2386–2395 (2014).
8. P. Gritsenko, W. Leenders, P. Friedl, Recapitulating in vivo-like plasticity of glioma cell invasion along blood vessels and in astrocyte-rich stroma. *Histochem. Cell Biol.* **148**, 395–406 (2017).
9. B. Weigelin, G. J. Bakker, P. Friedl, Intravital third harmonic generation microscopy of collective melanoma cell invasion: Principles of interface guidance and microvesicle dynamics. *IntraVital* **1**, 32–43 (2012).
10. A. J. Liu, S. R. Nagel, Jamming is not just cool any more. *Nature* **396**, 21–22 (1998).
11. E. Lawson-Keister, M. L. Manning, Jamming and arrest of cell motion in biological tissues. *Curr. Opin. Cell Biol.* **72**, 146–155 (2021).
12. K. Dozen *et al.*, Guidance of collective cell migration by substrate geometry. *Integr. Biol.* **5**, 1026–1035 (2013).
13. O. Chepizhko *et al.*, From jamming to collective cell migration through a boundary induced transition. *Soft Matter* **14**, 3774–3782 (2018).
14. C. Malinverno *et al.*, Endocytic reawakening of motility in jammed epithelia. *Nat. Mater.* **16**, 587–596 (2017).
15. P. Friedl, R. Mayor, Tuning collective cell migration by cell–cell junction regulation. *Cold Spring Harb. Perspect. Biol.* **9**, a029199 (2017).
16. O. Ilina *et al.*, Cell–cell adhesion and 3D matrix confinement determine jamming transitions in breast cancer invasion. *Nat. Cell Biol.* **22**, 1103–1115 (2020).
17. S. E. Leggett *et al.*, Mechanophenotyping of 3D multicellular clusters using displacement arrays of rendered tractions. *Proc. Natl. Acad. Sci. U.S.A.* **117**, 5655–5663 (2020).
18. G. Duclos, S. Garcia, H. Yevick, P. Silberzan, Perfect nematic order in confined monolayers of spindle-shaped cells. *Soft Matter* **10**, 2346–2353 (2014).
19. S. Garcia *et al.*, Physics of active jamming during collective cellular motion in a monolayer. *Proc. Natl. Acad. Sci. U.S.A.* **112**, 15314–15319 (2015).
20. W. D. Martinson *et al.*, Dynamic fibronectin assembly and remodeling by leader neural crest cells prevents jamming in collective cell migration. *eLife* **12**, e83792 (2023).
21. M. C. McKinney *et al.*, Visualizing mesoderm and neural crest cell dynamics during chick head morphogenesis. *Dev. Biol.* **461**, 184–196 (2020).
22. K. J. Painter, N. J. Armstrong, J. A. Sherratt, The impact of adhesion on cellular invasion processes in cancer and development. *J. Theor. Biol.* **264**, 1057–1067 (2010).
23. S. Sugeves, R. Eftimie, D. Trucu, Re-polarisation of macrophages within collective tumour cell migration: A multiscale moving boundary approach. *Front. Appl. Math. Stat.* **7**, 799650 (2022).
24. A. Doostmohammadi, I. Ignés-Mullol, J. M. Yeomans, F. Sagués, Active nematics. *Nat. Commun.* **9**, 3246 (2018).
25. L. Giomi, Geometry and topology of turbulence in active nematics. *Phys. Rev. X* **5**, 031003 (2015).
26. L. Balasubramanian *et al.*, Investigating the nature of active forces in tissues reveals how contractile cells can form extensible monolayers. *Nat. Mater.* **20**, 1156–1166 (2021).
27. I. Gromá, B. Bakó, Probability distribution of internal stresses in parallel straight dislocation systems. *Phys. Rev. B* **58**, 2969 (1998).
28. S. Henkes, Y. Fily, M. C. Marchetti, Active jamming: Self-propelled soft particles at high density. *Phys. Rev. E* **84**, 040301 (2011).
29. D. Bi, J. H. Lopez, J. M. Schwarz, M. L. Manning, A density-independent rigidity transition in biological tissues. *Nat. Phys.* **11**, 1074 (2015).
30. D. Bi, X. Yang, M. C. Marchetti, M. L. Manning, Motility-driven glass and jamming transitions in biological tissues. *Phys. Rev. X* **6**, 020111 (2016).
31. S. R. K. Vedula *et al.*, Emerging modes of collective cell migration induced by geometrical constraints. *Proc. Natl. Acad. Sci. U.S.A.* **109**, 12974–12979 (2012).
32. C. Leclerc *et al.*, Topography-induced large-scale antiparallel collective migration in vascular endothelium. *Nat. Commun.* **13**, 2797 (2022).
33. S. Alexander, G. E. Koehl, M. Hirschberg, E. K. Geissler, P. Friedl, Dynamic imaging of cancer growth and invasion: A modified skin-fold chamber model. *Histochem. Cell Biol.* **130**, 1147–1154 (2008).
34. A. Haeger *et al.*, Collective cancer invasion forms an integrin-dependent radioresistant niche. *J. Exp. Med.* **217**, e20181184 (2020).
35. B. Horn, B. Schunck, Determining optical flow. *Artif. Intell.* **17**, 185–203 (1981).
36. Z. Püspöki, M. Storath, D. Sage, M. Unser, Transforms and operators for directional bioimage analysis: A survey. *Focus Bio-image Inf.* **2016**, 69–93 (2016).
37. C. Joshi *et al.*, Data-driven discovery of active nematic hydrodynamics. *Phys. Rev. Lett.* **129**, 258001 (2022).